A statistical study of gamma-ray burst afterglows measured by the *Swift* Ultraviolet Optical Telescope

S. R. Oates,[1]* M. J. Page,[1] P. Schady,[1] M. de Pasquale,[1] T. S. Koch,[2]
A. A. Breeveld,[1] P. J. Brown,[2] M. M. Chester,[2] S. T. Holland,[3,4,5] E. A. Hoversten,[2]
N. P. M. Kuin,[1] F. E. Marshall,[3] P. W. A. Roming,[2] M. Still,[1] D. E. Vanden Berk,[2]
S. Zane[1] and J. A. Nousek[2]

[1]*Mullard Space Science Laboratory, University College London, Holmbury St. Mary, Dorking, Surrey RH5 6NT*
[2]*Department of Astronomy and Astrophysics, Pennsylvania State University, 104 Davey Laboratory, University Park, PA 16802, USA*
[3]*Astrophysics Science Division, Code 660.1, NASA Goddard Space Flight Centre, 8800 Greenbelt Road, Greenbelt, Maryland 20771, USA*
[4]*Universities Space Research Association, 10211 Wincopin Circle, Suite 500, Columbia, Maryland 21044, USA*
[5]*Centre for Research and Exploration in Space Science and Technology, Code 668.8, NASA Goddard Space Flight Centre, 8800 Greenbelt Road, Greenbelt, Maryland 20771, USA*

ABSTRACT

We present the first statistical analysis of 27 Ultraviolet Optical Telescope (UVOT) optical/ultraviolet light curves of gamma-ray burst (GRB) afterglows. We have found, through analysis of the light curves in the observer's frame, that a significant fraction rise in the first 500 s after the GRB trigger, all light curves decay after 500 s, typically as a power law with a relatively narrow distribution of decay indices, and the brightest optical afterglows tend to decay the quickest. We find that the rise could be either produced physically by the start of the forward shock, when the jet begins to plough into the external medium, or geometrically where an off-axis observer sees a rising light curve as an increasing amount of emission enters the observers line of sight, which occurs as the jet slows. We find that at 99.8 per cent confidence, there is a correlation, in the observed frame, between the apparent magnitude of the light curves at 400 s and the rate of decay after 500 s. However, in the rest frame, a Spearman rank test shows only a weak correlation of low statistical significance between luminosity and decay rate. A correlation should be expected if the afterglows were produced by off-axis jets, suggesting that the jet is viewed from within the half-opening angle θ or within a core of a uniform energy density θ_c. We also produced logarithmic luminosity distributions for three rest-frame epochs. We find no evidence for bimodality in any of the distributions. Finally, we compare our sample of UVOT light curves with the X-ray Telescope (XRT) light-curve canonical model. The range in decay indices seen in UVOT light curves at any epoch is most similar to the range in decay of the shallow decay segment of the XRT canonical model. However, in the XRT canonical model, there is no indication of the rising behaviour observed in the UVOT light curves.

Key words: gamma-rays: bursts.

1 INTRODUCTION

Gamma-ray bursts (GRBs) release between 10^{52} and 10^{54} erg during the prompt emission, which lasts from a few milliseconds to a few thousand seconds, and is followed by an afterglow, which is observed in the X-ray to radio range from as little as a few tens of seconds up to several months after the GRB trigger.

The energy is transported in a relativistic outflow (Meszaros & Rees 1997) that is likely anisotropic (Sari, Piran & Halpern 1999) and the energy is expected to be released by internal and external shocks. Internal shocks (Rees & Meszaros 1994) are thought to produce the prompt gamma-ray emission, while external shocks (Rees & Meszaros 1992) are thought to produce the afterglow. Internal shocks occur when shells of material, which are thrown

*E-mail: sro@mssl.ucl.ac.uk

violently from the progenitor at different Lorentz factors, overtake each other. The external shocks are produced when the shells of material are decelerated by the external medium.

The short duration of the gamma-ray emission and the rapid decay of the afterglow motivated the construction and launch of *Swift*, a rapid response satellite. *Swift* houses three instruments: the Burst Alert Telescope (BAT; Barthelmy et al. 2005), the X-ray Telescope (XRT; Burrows et al. 2005) and the Ultraviolet Optical Telescope (UVOT; Roming et al. 2005). The energy ranges of the BAT and XRT instruments are 15–350 and 0.2–10 keV, respectively, and the wavelength range of the UVOT is 1600–8000 Å. The large field of view of the BAT (2 sr) enables 1/6th of the sky to be searched for GRBs at any time. Once a GRB has been detected by the BAT, *Swift* rapidly slews allowing the XRT and UVOT to observe the afterglow within a few tens of seconds after the BAT trigger.

Since launch, *Swift* has produced a large sample of ultraviolet/optical (UV/optical) and X-ray light curves which begin soon after the trigger. The high detection rate with the XRT (96 per cent; Burrows et al. 2007) allowed a large number of XRT light curves to be obtained within the first year. The systematic reduction of this sample resulted in the discovery of a four segment canonical XRT light curve (Zhang et al. 2006; Nousek et al. 2006). After 2 yr of operation, the UVOT, with a much lower detection rate than the XRT (26 per cent; Roming et al. 2009), has detected more than 50 optical afterglows. This allows for the first time a systematic reduction and analysis of a significant sample of GRBs with optical afterglows observed with the UVOT and allows an investigation of their generic characteristics.

In this paper, we present and analyse a sample of 27 UVOT light curves of GRB afterglows. In Section 2, we explain how we selected the sample of UVOT light curves and in Section 3 we describe how we systematically reduced and analysed them. In Section 4, we present the results and in Section 5 we discuss our findings. Throughout the paper, we will use the following flux convention, $F \propto t^{\alpha} \nu^{\beta+1}$ with α and β being the temporal and photon indices, respectively. We assume the Hubble parameter $H_0 = 70 \, \mathrm{km \, s^{-1} \, Mpc^{-1}}$ and density parameters $\Omega_{\Lambda} = 0.7$ and $\Omega_{\mathrm{m}} = 0.3$. Unless stated otherwise, all uncertainties are quoted at 1σ.

2 THE SAMPLE

To investigate the nature of GRB optical/UV light curves, a large number of well-sampled, good quality UVOT light curves were required. The sample was selected according to the following specific criteria: the optical/UV light curves must be observed in the v filter of the UVOT with a magnitude of ≤ 17.8, UVOT observations must have commenced within the first 400 s after the BAT trigger and the afterglow must have been observed until at least 10^5 s after the trigger. These selection criteria ensure the light curves have adequate signal-to-noise ratio and cover both early- and late-time evolution. In addition to the above criteria, the colour of the afterglows must not evolve significantly with time, meaning that at no stage should the light curve from a single filter significantly deviate from any of the other filter light curves when normalized to the v filter. This ensures that a single light curve can be constructed from the UVOT multifilter observations. Three GRBs, GRB 060218, GRB 060614 and GRB 060729, were excluded as they showed significant colour evolution.

In total 27 GRBs, which occurred between 2005 January 1 and 2007 August 1, fit the selection criteria. As there were no short GRBs that met the selection criteria, all the GRBs in this sample are long. Observations, for the majority of GRBs in this sample, began within the first 100 s and the optical afterglow was detected until at least 10^5 s. Formally, GRB 050820a meets our selection criteria, but we have excluded this burst from the sample because the BAT triggered on a precursor of this GRB, and the main GRB took place as *Swift* entered the South Atlantic Anomaly with the consequence that UVOT completely missed the early phase of the afterglow.

3 DATA REDUCTION

After the BAT has triggered on a GRB and *Swift* has slewed, the UVOT performs a sequence of pre-programmed exposures of varying length in multiple observing modes and filters designed to balance good time resolution and spectral coverage. Observations are performed in either event mode, where the arrival time and position are recorded for every photon detected, or image mode, in which the data are recorded as an image accumulated over a fixed period of time. The pre-programmed observations begin with the settling and finding chart exposures. The settling exposure is not included in this analysis because the cathode voltage may still increase during the first few seconds. Two finding charts follow immediately after the settling exposure and these are observed in event mode with the v and white filters (as of the 2008 November 7, the finding charts are observed in u and white). The rest of the pre-programmed observations are a combination of event and image mode observations until ~2700 s after the trigger, after which, only image mode is used. These observations are taken as a series of short, followed by medium and then long exposures, which are usually observed with all seven filters of the UVOT (white, v, b, u, $uvw1$, $uvm2$ and $uvw2$). However, for some targets, the pre-programmed observation sequence may change or not be executed fully because of an observing constraint.

For GRB observations, the earliest part of the light curve is expected to show variability over the shortest time-scales. As the finding charts, which are exposures of 100–400 s, contain the earliest observations of the GRB, it is essential to obtain light curves from these event lists as well as obtaining light curves from the images.

3.1 Event and image data reduction

To obtain the best possible light curves, we refined the astrometry of the event files before the count rates were obtained. The astrometry of the event list was refined by extracting an image every 10 s and cross-correlating the stars in the image with those found in the USNO-B1 catalogue. The differences in RA and Dec. between the stars in the image and the catalogue were converted into pixels and then applied to the position of every event in the event list during that particular 10 s interval. This process was repeated until the end of each event list.

The images used in this paper were reprocessed by the *Swift* Science Data Center (SDC) for the UVOT GRB catalogue (Roming et al. 2009). These images were used because not all the image files in the *Swift* archive have been corrected for modulo-8 fixed pattern noise;[1] only those processed with *Swift* processing script version 3.9.9 and later have had this correction applied. For a small number of images, the aspect correction failed during the SDC processing and in these cases, the images were corrected using in-house aspect correction software.

---

[1] http://heasarc.nasa.gov/docs/swift/analysis/UVOT_swguide_v2_2.pdf

An aperture of 5 arcsec, selected in order to be compatible with the UVOT calibration (Poole et al. 2008), was used to obtain the source count rates. However, for sources with a low count rate, it is more precise to use a smaller aperture (Poole et al. 2008). Therefore, below a threshold of 0.5 counts per second, the source count rates were determined from 3 arcsec radius apertures and the count rates were corrected to 5 arcsec using a table of aperture correction factors contained within the calibration. The background counts were obtained from circular regions with radii, typically, of 20 arcsec. These regions were positioned, in each GRB field, over a blank area of sky. For each GRB, the same source and background regions were used to determine the count rates from the event lists and images. The software used can be found in the software release, HEADAS 6.3.2 and the version 20071106 of the UVOT calibration files.

For each GRB, to maximize the signal-to-noise ratio of the observed optical afterglow, the light curves from each filter in which the burst was detected were combined into one overall light curve. The light curves corresponding to the different filters were normalized to that in the v filter. This was possible because there was no significant colour evolution between the filters, which was one of the selection criteria described in Section 2. The normalization was determined by fitting a power law to each of the light curves in a given time range simultaneously. The power-law indices were constrained to be the same for all the filters and the normalizations were allowed to vary between the filters. The ratios of the power-law normalizations were then used to normalize the count rates in each filter. The time range used to normalize the light curves was selected on the basis that the time range included data from all filters in which the burst was detected and (as far as possible) the light curves were in a power-law decay phase. Once the light curves were normalized, they were binned by taking the weighted average of the normalized count rates in time bins of $\delta T/T = 0.2$. The overall light curves were converted from v count rate to v magnitude using the zero point 17.89 (Poole et al. 2008). For many GRBs, the trigger time does not represent the true start of the gamma-ray emission. Therefore, the start of the gamma-ray emission was chosen as the start time of the T90 parameter. This parameter corresponds to the time in which 90 per cent of the counts in the 15–350 keV band arrive at the detector (Sakamoto et al. 2008a) and is determined from the gamma-ray event data for each GRB, by the BAT processing script. The results of the processing are publicly available and provided for each trigger at http://gcn.gsfc.nasa.gov/swift_gnd_ana.html. The difference between the trigger time and the start time of the T90 parameter is typically less than a few seconds. However, in a minority of cases, the difference is much larger, with the largest difference being 133.1 s for GRB 050730.

3.2 Photometric redshifts

Spectroscopic redshifts were obtained from the literature for 19 of the GRBs in the sample (see Table 1). For further four GRBs, it was possible to determine the redshift using an instantaneous UVOT–XRT spectral energy distribution (SED), which was created using the method of Schady et al. (2009). The SEDs were fit with the best-fitting model of either a power law or broken power law, with Galactic and host galaxy absorption and extinction. The Galactic $N_{\rm H}$ was taken from the Leiden/Argentine/Bonn (LAB) survey of Galactic H I (Kalberla et al. 2005) and the Galactic extinction was taken from a composite $100\,\mu{\rm m}$ map of *COBE*/Diffuse Infrared Background Experiment (*COBE*/DIRBE) and *IRAS*/ISSA observations (Schlegel, Finkbeiner & Davis 1998).

Table 1. Spectroscopic redshifts were largely taken from the literature. For four GRBs, photometric redshifts, indicated by an *, were determined using the XRT–UVOT SEDs (see Section 3 for more details). The host extinction values at 1600 Å were calculated from the best fit A_v given in Schady et al. (2009). The count rate relative to v is provided for each filter detected by the UVOT. For a few GRBs, there were no observations with the white filter and for GRB 060804, the white data could not be used; the white column for these GRBs contains N/A.

| GRB | Redshift | A_{1600} | Count rate relative to v | | | | | |
			b	u	$w1$	$m2$	$w2$	White
050319	3.24^a	0.27	1.36	–	–	–	–	N/A
050525	0.606^b	0.25	2.29	2.72	1.05	0.46	0.56	4.59
050712	–	–	–	0.68	–	–	–	N/A
050726	–	–	0.63	–	–	–	–	N/A
050730	3.97^c	0.64	0.78	–	–	–	–	N/A
050801	1.38^*	0.00	2.25	2.46	0.81	0.29	0.13	N/A
050802	1.71^d	0.47	2.75	2.34	0.52	0.05	0.07	4.79
050922c	2.198^e	0.35	1.99	1.83	0.11	–	–	N/A
051109a	2.346^f	0.04	1.98	0.88	0.21	–	–	7.96
060206	4.04795^g	0.00	0.42	–	–	–	–	N/A
060223a	4.41^h	–	0.26	–	–	–	–	4.18
060418	1.4901^i	0.34	1.82	1.40	0.36	0.07	0.06	6.21
060512	0.4428^j	1.93	3.03	2.31	0.20	–	–	8.46
060526	3.221^k	0.00	1.39	–	–	–	–	2.99
060605	3.8^l	1.08	0.79	–	–	–	–	2.74
060607a	3.082^m	0.21	1.56	0.19	–	–	–	4.36
060708	1.92^*	0.56	1.85	1.76	0.25	–	–	7.49
060804	–	–	2.10	0.00	–	–	–	N/A
060908	2.43^n	0.08	2.07	2.23	0.40	–	–	9.27
060912	0.937^o	2.09	1.58	2.16	0.41	0.17	0.27	8.83
061007	1.262^p	2.77	1.84	1.35	0.25	0.07	0.06	6.03
061021	0.77^*	0.00	2.38	3.14	1.74	0.81	1.23	11.97
061121	1.314^q	1.35	2.70	2.45	0.58	0.17	0.14	9.03
070318	0.836^r	1.72	1.75	1.50	0.29	0.08	0.07	6.69
070420	3.01^*	1.53	1.52	0.47	0.19	–	–	6.35
070529	2.4996^s	0.57	3.42	0.92	–	–	–	N/A

Notes. References: (a) Jakobsson et al. (2006a), (b) Foley et al. (2005), (c) Chen et al. (2005), (d) Fynbo et al. (2005), (e) Jakobsson et al. (2006a), (f) Quimby et al. (2005), (g) Fynbo et al. (2006), (h) Berger et al. (2006), (i) Prochaska et al. (2006), (j) Bloom et al. (2006), (k) Jakobsson et al. (2006a), (l) Peterson & Schmidt (2006), (m) Ledoux et al. (2006), (n) Rol et al. (2006), (o) Jakobsson et al. (2006c), (p) Jakobsson et al. (2006b), (q) Bloom, Perley & Chen (2006), (r) Jaunsen et al. (2007) and (s) Berger, Fox & Cucchiara (2007).

For the host extinction, the Small Magellanic Cloud extinction curve (Pei 1992) was assumed. The host reddening and absorption, $E(B - V)$, $N_{\rm H}$ and the redshift were left to vary. The resulting redshifts can be found in Table 2.

3.3 Luminosity light curve

Luminosity light curves were produced for all the GRBs whose host $E(B - V)$ value could be determined, except for GRBs with

Table 2. Photometric redshifts for four of the GRBs without spectroscopic redshifts.

GRB	Photometric redshift	χ^2/d.o.f.
GRB 050801	1.38 ± 0.07	(14/12)
GRB 060708	1.92 ± 0.12	(21/20)
GRB 061021	$0.77^{+0.06}_{-0.01}$	(229/174)
GRB 070420	$3.01^{+0.96}_{-0.68}$	(58/60)

photometric redshifts which have a 1σ error on the redshift that corresponds to an uncertainty in log luminosity of >0.1. In total, luminosity light curves were produced for 21 of the GRBs in the sample.

For the 21 GRBs, the observed count rate was converted into luminosity at a common rest-frame wavelength. In order to select the common wavelength and determine the resulting k-correction factor for each light curve, an SED was computed for each GRB. The SED was produced by multiplying the relative count rates in each filter, given in Table 1, by the count-rate-to-flux-conversion factors given by Poole et al. (2008). These relative flux densities were corrected for Galactic extinction and positioned at the central wavelength of the filter in the rest frame of the GRB; the SEDs are shown in Fig. 1. The common rest-frame wavelength at which to determine the luminosities was selected to maximize the number of GRBs with SEDs that include this wavelength and to be relatively unaffected by host extinction. The wavelength which best satisfies these conditions is 1600 Å. The k-correction factor was taken as the flux density in the rest frame at 1600 Å, F_{1600}, divided by the flux density at the observed central wavelength of the v filter (5402 Å), F_v. In the case where a GRB's SED did not cover 1600 Å, an average k-correction was determined from the other GRBs in the sample, whose SEDs covered both 1600 Å and the rest-frame wavelength corresponding to the v filter.

To produce the luminosities, the light curves in count rate were corrected for Galactic extinction, converted into flux density and then into luminosity using the following equation:

$$L(1600) = 4\pi D_L^2 F_v k, \qquad (1)$$

where $L(1600)$ is the luminosity at a 1600 Å, D_L is the luminosity distance, $k = (1 + z)(F_{1600}/F_v)$ is the k-correction factor and z is the redshift of the GRB. Finally, the luminosity light curves were corrected for host extinction using the A_{1600} values given in Table 1. These values were determined for the GRBs, using the A_v values reported in Schady et al. (2009).

3.4 Bolometric energy and GRB classification

The k-corrected isotropic energy of the prompt gamma-ray emission, $E_{k,\mathrm{iso}}$, was calculated for each GRB with known redshift using equation (4) from Bloom, Frail & Sari (2001). The energies were corrected to a rest-frame bandpass of 0.1 to 10 000 keV using one of three spectral templates: a power law, cut-off power law or band function (Band et al. 1993). As Konus–Wind has a larger energy range than BAT, the spectral analysis of the prompt emission, observed by Konus–Wind, better represents the spectral behaviour. These results were taken from the literature. The spectra observed with Konus–Wind tend to be best fit by a cut-off power law; therefore, the spectral template chosen for the GRBs that were not observed with Konus–wind, with power-law spectra of photon index $\Gamma > -2$ in the 15–150 keV energy range, was a cut-off power law with $E_{\mathrm{peak}} = 162.2$ keV (D'Alessio, Piro & Rossi 2006). For the GRBs with a power-law spectrum with a photon index of $\Gamma < -2$ in the 15–150 keV energy range, a band function was used with $\Gamma_1 = -0.99$ (D'Alessio et al. 2006) and $E_{\mathrm{peak}} = 15$ keV. The resulting k-corrected energies can be found in Table 3.

The GRBs in this sample were classified into three categories depending on the ratio R of the fluence in the 25–50 and 50–100 keV BAT energy bands, which are given in Sakamoto et al. (2008b). The categories and their respective ratios are: an X-ray flash (XRF) for $R > 1.32$; an X-ray rich GRB (XRR) for $0.72 < R \le 1.32$ or a classical GRB (C-GRB) for $R \le 0.72$. Table 4 lists the GRBs with their classifications. In total, there are 12 C-GRBs, 13 XRR and 1 XRF, which is GRB 060512.
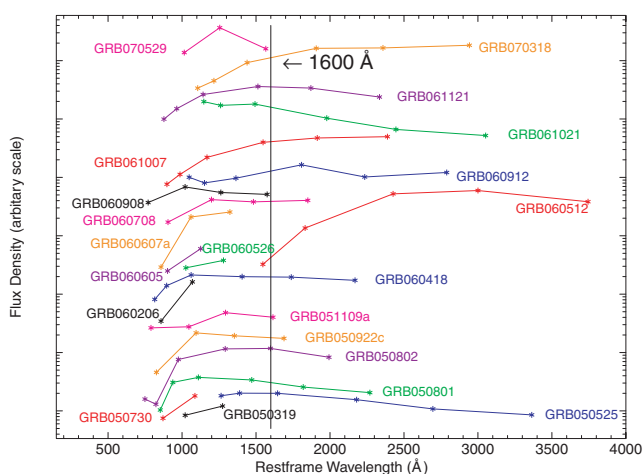

Figure 1. The (scaled) rest-frame relative flux SEDs for the 21 GRBs for which a luminosity light curve was produced. The relative flux for each filter of each GRB was determined by multiplying the relative count rate from Table 1 by the flux conversion factor given in Poole et al. (2008). The relative flux values have been corrected for Galactic extinction. The vertical line at 1600 Å marks the rest-frame wavelength at which the luminosity light curves were produced.

Table 3. Properties of the GRBs with spectroscopic or photometric redshifts. This table contains the luminosity distance, the gamma-ray photon indices and peak energies used to determine the k-corrected isotropic energy for each GRB in the energy range 10–10 MeV.

GRB		D_L (cm)	β_1	β_2	E_{peak}	$E_{\mathrm{iso},k}$
050319	BAND	8.60×10^{28}	-0.99	-2.02^a	162.0	1.44e+53
050525	CPL	1.10×10^{28}	-1.10^b	-2.31	84.1^b	1.59e+53
050730	CPL	1.04×10^{29}	-1.53^a	-2.31	162.2	3.85e+54
050801	CPL	3.04×10^{28}	-1.99^a	-2.31	162.2	7.67e+53
050802	CPL	3.96×10^{28}	-1.54^a	-2.31	162.2	5.86e+53
050922c	CPL	5.38×10^{28}	-1.55^c	-2.31	162.2	4.30e+54
051109a	CPL	5.82×10^{28}	-1.25^d	-2.31	161.0^d	6.43e+53
060206	CPL	1.12×10^{29}	-1.20^a	-2.31	78.0^a	3.42e+53
060223a	CPL	1.24×10^{29}	-1.74^a	-2.31	162.2	4.47e+54
060418	CPL	3.34×10^{28}	-1.50^e	-2.31	230.0^e	2.94e+54
060512	BAND	7.56×10^{27}	-0.99	-2.48^a	162.2	5.04e+50
060526	BAND	8.54×10^{28}	-0.99	-2.01^a	162.2	1.37e+53
060605	CPL	1.04×10^{29}	-1.55^a	-2.31	162.2	1.15e+54
060607a	CPL	8.10×10^{28}	-1.47^a	-2.31	162.2	1.81e+54
060708	CPL	4.56×10^{28}	-1.68^a	-2.31	162.2	3.79e+53
060908	CPL	6.08×10^{28}	-1.00^a	-2.31	151.0^a	1.88e+53
060912	POWER	1.88×10^{28}	-1.74^f	-2.31	162.2	2.52e+54
061007	BAND	2.72×10^{28}	-0.70^g	-2.61^g	399.0^g	2.00e+53
061021	CPL	1.48×10^{28}	-1.22^h	-2.31	777.0^h	9.65e+52
061121	CPL	2.86×10^{28}	-1.32^i	-2.31	606.0^i	2.75e+54
070318	CPL	1.63×10^{28}	-1.42^a	-2.31	162.2	8.78e+52
070420	CPL	7.87×10^{28}	-1.23^j	-2.31	147.0^j	6.39e+54
070529	CPL	6.14×10^{28}	-1.34^a	-2.31	162.2	6.46e+53

Notes. References: [a]Sakamoto et al. (2008a), [b]Golenetskii et al. (2005a), [c]Golenetskii et al. (2005b), [d]Golenetskii et al. (2005c), [e]Golenetskii et al. (2006e), [f]Golenetskii et al. (2006b), [g]Golenetskii et al. (2006c), [h]Golenetskii et al. (2006d), [i]Golenetskii et al. (2006a) and [j]Golenetskii et al. (2007).

Table 4. The v peak magnitude, peak time and best-fitting decay indices of the light curves before and after 500 s and the classification of each GRB. In the cases where a peak was not observed, an upper limit to the peak time is provided. The GRBs are classified into three categories depending on the ratio of the fleuence in the 25–50 and 50–100 keV BAT energy bands, which are given in Sakamoto et al. (2008a): an X-ray flash (XRF), an X-ray rich GRB (XRR) or a classical GRB (C-GRB).

Name	Classification	Peak magnitude	Peak time (s)	$\alpha_{<500\,s}$	$(\chi^2/\text{d.o.f.})$	$\alpha_{>500\,s}$	$(\chi^2/\text{d.o.f.})$
050319	XRR	17.09	<234	0.09 ± 0.35	0/ 2	-0.63 ± 0.03	34/17
050525	XRR	13.57	<78	-1.25 ± 0.03	21/ 9	-1.00 ± 0.01	398/26
050712	C-GRB	17.77	<178	0.11 ± 0.64	4/ 3	-0.50 ± 0.05	52/26
050726	C-GRB	17.21	<159	-2.67 ± 0.80	1/ 3	0.13 ± 0.29	21/13
050730	C-GRB	17.22	744	0.15 ± 0.50	6/ 3	-0.89 ± 0.05	72/16
050801	XRR	15.26	<66	-0.46 ± 0.04	43/10	-1.17 ± 0.03	41/15
050802	XRR	17.07	<289	0.07 ± 0.48	0/ 1	-0.75 ± 0.01	53/29
050922c	C-GRB	14.34	<109	-1.01 ± 0.05	21/ 6	-0.94 ± 0.01	88/14
051109a	C-GRB	16.33	<122	-0.47 ± 0.45	0/ 2	-0.68 ± 0.02	80/16
060206	XRR	16.64	<57	-0.02 ± 0.50	9/ 4	-0.70 ± 0.03	205/22
060223a	XRR	17.33	<88	-1.06 ± 0.33	4/ 6	-1.53 ± 0.60	31/14
060418	XRR	14.69	260	0.01 ± 0.03	138/ 6	-1.22 ± 0.01	58/21
060512	XRF	16.50	<114	-0.74 ± 0.08	3/ 6	-0.99 ± 0.05	10/14
060526	XRR	16.59	<82	-0.29 ± 0.08	36/ 8	-0.69 ± 0.02	141/22
060605	XRR	16.50	459	0.26 ± 0.13	6/ 4	-0.94 ± 0.03	27/11
060607a	C-GRB	14.50	254	0.50 ± 0.03	702/ 8	-1.17 ± 0.03	152/20
060708	XRR	17.19	<72	-0.10 ± 0.10	8/ 9	-0.89 ± 0.03	39/23
060804	XRR	17.43	<231	-1.76 ± 0.49	0/2	-0.57 ± 0.08	21/9
060908	C-GRB	15.21	<88	-1.19 ± 0.05	6/ 8	-1.03 ± 0.04	20/18
060912	XRR	16.44	<114	-0.97 ± 0.09	2/ 6	-0.53 ± 0.01	149/27
061007	C-GRB	12.68	<298	-1.63 ± 0.11	1/ 1	-1.59 ± 0.01	129/28
061021	C-GRB	15.64	<79	-0.92 ± 0.06	3/ 9	-0.88 ± 0.01	556/29
061121	C-GRB	15.67	<53	-0.12 ± 0.05	181/11	-0.67 ± 0.01	179/31
070318	C-GRB	15.37	316	0.42 ± 0.03	19/ 9	-1.02 ± 0.01	261/27
070420	C-GRB	17.16	347	0.73 ± 0.14	13/ 5	-1.67 ± 0.15	56/23
070529	C-GRB	15.95	<131	-1.64 ± 0.14	5/ 5	-0.53 ± 0.04	42/19

4 RESULTS

In this section, the flux light curves in the observer frame and their properties will be investigated first, then the luminosity light curves in the rest frame and their properties will be examined.

4.1 Observer frame flux light curves

The light curves, shown in Fig. 2, are ordered by peak magnitude from the brightest, GRB 061007, to the faintest, GRB 050712. Data points with signal-to-noise ratio below 2 are shown as 3σ upper limits. The peak magnitude was taken as the maximum magnitude in each binned light curve and given in Table 4. A trend is observed in the figure, with the brightest GRBs decaying more quickly than the faintest GRBs. The light curves generally follow one of two types of behaviour. Either they rise to a peak within the first 1000 s and then decay, or they decay from the beginning of the observations. There are six light curves that appear to rise to a peak between 200 and 1000 s after the burst trigger. The peak times for the six GRBs were determined from a Gaussian fit to each light curve in log time. The fit was performed between the brightest data point and the data points on either side to the point at which the count rate is 60 per cent of the peak value. The mean of these peak times is 397 s. For the remaining GRBs, the beginning of the light curve was taken as the upper limit to the peak time and the mean of these upper limits is 132 s.

To classify the behaviour of the light curves, two power laws were fit to each light curve, covering the time ranges from the start of observations until 500 s and from 500 s until the end of the

observations; the results are given in Table 4. A time of 500 s was chosen as it ensures that the early power-law fits are performed on at least 100 s of each light curve and because the rising phase tends to occur during the first 500 s.

A comparison of the temporal indices before and after 500 s is shown in Fig. 3. The figure is divided into three groups of behaviour, which are: light curves which rise before 500 s, light curves which decay more steeply after 500 s and light curves which decay less steeply after 500 s. Each of these groups contains a similar number of GRBs. From Fig. 3, there are four light curves that are clearly rising with an $\alpha_{<500\,s}$ ranging from 0.26 ± 0.13 (GRB 060605) to 0.73 ± 0.14 (GRB 070420). Further seven light curves are consistent with $\alpha_{<500\,s} \sim 0$ or have large errors and thus it is not clear if these light curves are rising, constant or decaying before 500 s. The remaining 15 light curves decay with temporal indices of between $\alpha_{<500\,s} = -0.12 \pm 0.05$ (GRB 061121) and $\alpha_{<500\,s} = -2.67 \pm 0.80$ (GRB 050726). After 500 s, all the light curves decay with values of $\alpha_{>500\,s}$ ranging from -0.50 ± 0.05 (GRB 050712) to -1.67 ± 0.15 (GRB 070420), except for GRB 050726 where, due to the poor signal-to-noise ratio, it is not possible to tell if the light curve after 500 s is rising or decaying.

The mean and intrinsic dispersion of the temporal indices was determined using the maximum likelihood method (Maccacaro et al. 1988), which assumes a Gaussian distribution. The mean for $\alpha_{<500\,s}$ is $-0.48^{+0.15}_{-0.19}$ with a dispersion of $0.69^{+0.19}_{-0.06}$ and the mean for $\alpha_{>500\,s}$ is $-0.88^{+0.08}_{-0.07}$ with a dispersion of $0.31^{+0.07}_{-0.03}$. To see if $\alpha_{<500\,s}$ and $\alpha_{>500\,s}$ are independent parameters, a Spearman rank test was performed. This test gives a coefficient of -0.22 with a probability of 73 per cent, indicating no evidence for a correlation and suggesting
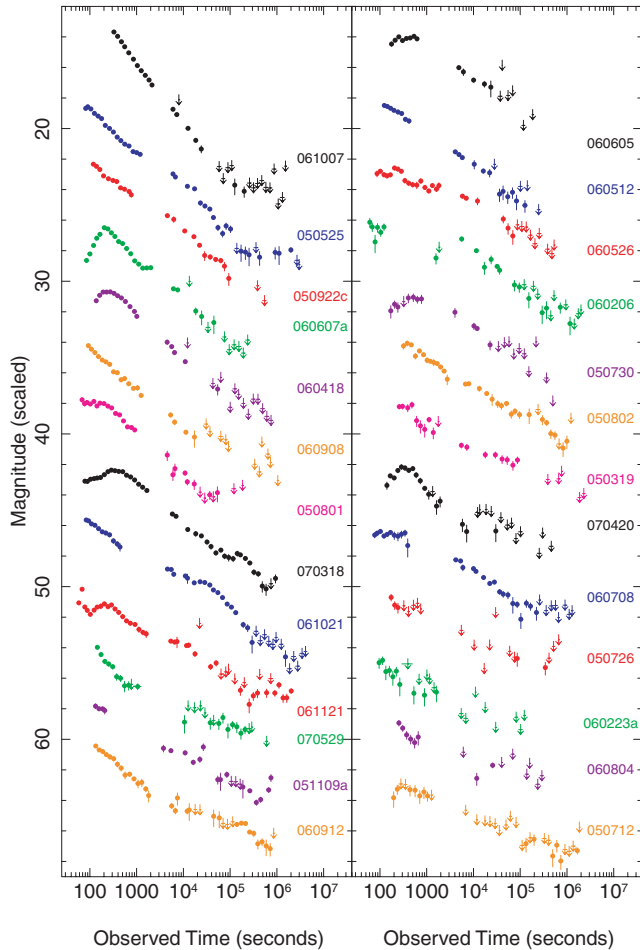
Figure 2. The light curves ordered by peak magnitude from brightest (GRB 061007) to faintest (GRB 050712). With a few exceptions, the light curves also appear to be ordered by decay rate with the brighter bursts decaying more rapidly than the fainter bursts. The down arrows in each light curve represent 3σ upper limits.

Figure 3. Temporal decay after 500 s versus temporal decay before 500 s. The dashed (red) line indicates the point at which the temporal index before 500 s equals the temporal index after 500 s. The dash–dotted (green) line indicates the cut off between GRBs that rise within the first 500 s (above the line) and GRBs that decay within the first 500 s (below the line).

that the behaviour after 500 s is independent of the behaviour before 500 s.

Since the light curves in Fig. 2 suggest a connection between the brightness and the decay rate, a Spearman rank correlation was performed between the temporal indices and the interpolated magnitudes of the light curves at 400 s. The test performed between $\alpha_{<500\,s}$ and the magnitude at 400 s indicates that these parameters are not related, as the coefficient is -0.28 at 84 per cent confidence. However, the Spearman rank test performed on $\alpha_{>500\,s}$ and the magnitude at 400 s gives a coefficient of 0.59 at 99.8 per cent confidence (see Fig. 4). The correlation is statistically significant at $>3\sigma$ and therefore implies that brighter GRBs tend to have faster decays.

The mean redshifts of the two columns in Fig. 2 are $\langle z \rangle = 1.63$ and 2.98, suggesting that the decay rate and magnitude are also correlated with redshift because the optical afterglows that are brighter and decay more steeply tend to have lower redshifts. A Spearman rank test performed between $\alpha_{>500\,s}$ and redshift gives no evidence for a correlation with a correlation coefficient of 0.07 and a insignificant probability of 23 per cent. However, a Spearman rank test performed between the redshift and magnitude at 400 s, provides a weak correlation with a coefficient of 0.32 and a statistical significance of 87 per cent. Moreover, if the Spearman rank test is
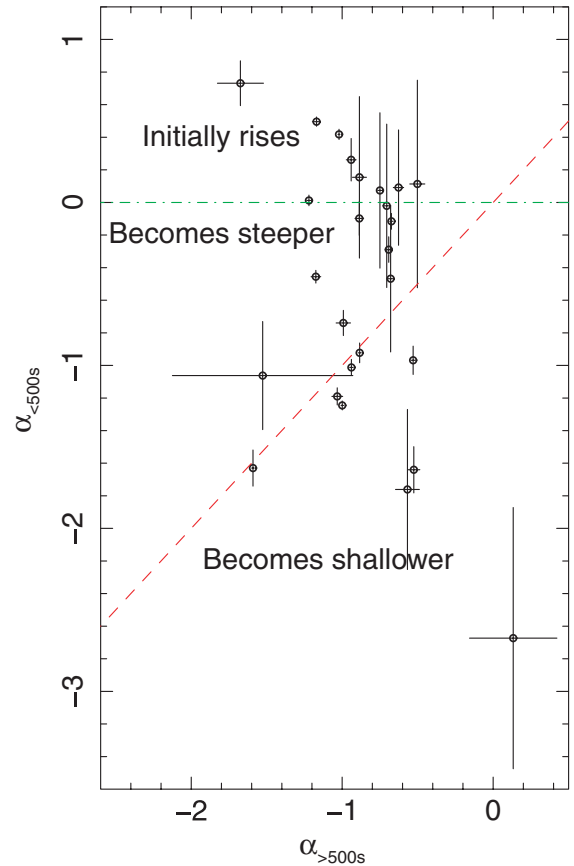
performed between the peak magnitude and redshift, the link between the redshift and magnitude is stronger and more significant as the coefficient is 0.55 and the confidence is 99.3 per cent. These correlations imply that the correlation between magnitude at 400 s and $\alpha_{>500\,s}$ is only weakly dependent on redshift.

The light curves of the GRBs after 500 s, in a few cases, appear to show a change in their temporal behaviour. To quantify this behaviour, a broken power law was fitted to each GRB from 500 s until the end of the observations. The broken power law is considered an improvement if the χ^2/d.o.f. has decreased and the probability of chance improvement is small (<1 per cent), as determined using an F-test. In five cases, a broken power law was an improvement compared with a single power law. The results of the broken power-law fits for the five GRBs are given in Table 5. In four of these five cases, the broken power law shows a transition from a shallow to a steeper decay. In the fifth case, GRB 070318, the decay became shallower at late times. To test if a single break is sufficient for the decay after 500 s, a doubly broken power law was fit to these five GRBs. As with the broken power law, the doubly broken power law was considered an improvement if the χ^2/d.o.f. decreased and the probability of chance improvement is small (<1 per cent). The doubly broken power law was an improvement for only GRB 070318. The best-fitting values for this model are: $\alpha_1 = -1.08 \pm 0.01$, $t_{break,1} = 53800^{+6800}_{-6100}$, $\alpha_2 = -0.11^{+0.12}_{-0.14}$, $t_{break,2} = 197000^{+22000}_{-15000}$, $\alpha_3 = -1.72 \pm 0.18$ with χ^2/d.o.f. $= 62/23$.
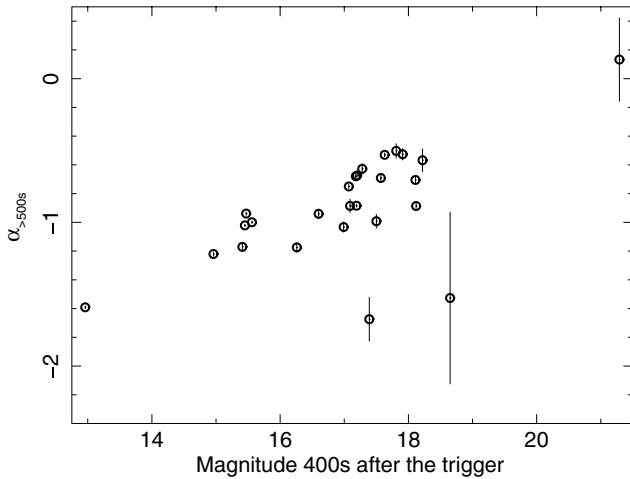
Figure 4. Magnitude at 400 s against the temporal index after 500 s, $\alpha_{>500\,s}$. A Spearman rank correlation test performed on these parameters gives a coefficient of 0.59 at a statistical significance of 99.8 per cent, indicating that these two parameters are correlated.

For the four GRBs where the broken power law was the best fit, the mean decay index before the break is -0.60 ± 0.14 with a dispersion of $0.19^{+0.18}_{-0.07}$ and the mean decay index after the break is -1.53 ± 0.19 with a dispersion of $0.22^{+0.28}_{-0.09}$. The break times range from 6000^{+1000}_{-1100} to $(4.9 \pm 0.25) \times 10^4$ s. If the mean decay index after 500 s is recalculated including only those light curves that decay as a single power law after 500 s, the mean is $-0.87^{+0.10}_{-0.09}$ with a dispersion of $0.35^{+0.10}_{-0.04}$. This mean is similar to the mean decay index determined using all the GRBs in the sample. For the light curves that show a break, the mean decay before the break is consistent within 2σ with these mean values.

4.2 GRB rest-frame luminosity light curves

The luminosity light curves at 1600 Å, in units of erg s^{-1} cm^{-1} Å^{-1}, before and after correction for host extinction, are shown in Fig. 5. Panel (a) shows the luminosity light curves before any correction for the host extinction has been applied. In both panels of Fig. 5, GRB 060512 lies significantly below all the other light curves. We suspect that this is caused by an incorrect determination of either the host extinction or the redshift. The redshift of this GRB could be wrong because it was not determined from the afterglow spectra, but was based on the alignment of the GRB with a galaxy (Bloom et al. 2006). In Schady et al. (2009), the best-fitting model to the SED of GRB 060512 gives a poor fit with a χ^2/d.o.f. $= 84/23$ and a host extinction of $E(B - V)_{\rm host} = 0.16^{+0.01}_{-0.00}$. A photometric

redshift was determined for this GRB using the method described in Section 2, of $z = 2.279^{+0.09}_{-0.18}$ and an extinction of $A_{1600} = 0.00^{+0.02}_{-0.00}$. Using these values, a luminosity light curve for GRB 060512 at 1600 Å was produced. This photometric redshift changes the rest-frame relative flux SED and consequently the k-correction factor. The result is that the luminosity light curve increases by ~ 3 orders of magnitude, which means that this GRB is no longer separated from the rest of the GRBs in the sample. None the less, this GRB may be intrinsically different to all the other GRBs in the sample as this GRB is the only XRF in the sample and it may be that XRFs are a class of subluminous GRBs. However, as it is uncertain whether the redshift of GRB 060512 is correct, the luminosity light curve for this GRB will be excluded from any further analysis.

To produce luminosity distributions, the luminosities were interpolated from the light curves before and after correction for host extinction at the three rest-frame epochs: 100 s, 1000 s and 10 ks. The logarithmic distribution of the luminosities at the three epochs are shown in panels (a) to (f) of Fig. 6. The distributions consisting of the luminosities at 100 s contain 18 GRBs whereas the distributions for the luminosities at 1000 s and 10 ks contain 20 GRBs. Panels (a) to (c) show the logarithmic distribution of luminosities before correction for host extinction. The means of these distributions at 100 s, 1000 s and 10 ks in the rest frame are 11.08, 10.29 and 9.39, respectively. The standard deviations at the three rest-frame epochs are 0.65 at 100 s, 0.71 at 1000 s and 0.68 at 10 ks. Panels (d) to (f) show the logarithmic distributions of the luminosity light curves that have been corrected for host extinction. The mean of the host extinction corrected distributions at 100 s, 1000 s and 10 ks in the rest frame is 11.29, 10.55 and 9.64, respectively, and the standard deviations are 0.57 at 100 s, 0.67 at 1000 s and 0.62 at 10 ks.

The distribution of rest-frame peak times and upper limits is shown in Fig. 7. The peak times of the GRBs with observed peaks overlap with the upper limits of the GRBs without observed peaks. Therefore, it is not possible to tell if the GRBs with observed peaks are a separate class, or if they belong to the tail end of a distribution where the majority of GRB peaks occur before the UVOT can observe them.

To determine if the relationship between the brightness of the afterglow and the late-time decay rate is intrinsic, the luminosity light curves were fitted with a power law from 150 s onwards $\alpha_{>150s,rest}$, where 150 s $\simeq 500$ s$/(1 + \langle z \rangle)$ and $\langle z \rangle = 2.21$ is the mean redshift of the GRBs in the sample, and a Spearman rank test was performed between this decay and the extinction-corrected luminosity at 100 s in the rest frame. These parameters are shown in Fig. 8. The Spearman rank test does not support or refute a correlation between these parameters because the coefficient is -0.29 and the probability of correlation is not significant at 76 per cent.

Table 5. Five of the light curves in the sample could be fit with a broken power law from 500 s onwards. The final column provides the difference in χ^2 (for two additional degrees of freedom) when fitting the light curve after 500 s with a single and broken power laws.

GRB	α_1	Break time	α_2	(χ^2/d.o.f.)	$\Delta\chi^2$
GRB 050525	-0.80 ± 0.01	16400^{+1200}_{-1400}	-1.70 ± 0.08	(120/24)	278
GRB 050922c	-0.76 ± 0.03	6000^{+1100}_{-1000}	-1.20 ± 0.05	(16/12)	59
GRB 060526	-0.33 ± 0.04	30800^{+4700}_{-5800}	$-2.33^{+0.65}_{-0.47}$	(32/20)	93
GRB 061021	-0.51 ± 0.02	49300^{+2500}_{-2500}	$-1.60^{+0.07}_{-0.06}$	(49/27)	507
GRB 070318	-1.09 ± 0.01	16000^{+3600}_{-3000}	-0.78 ± 0.03	(131/25)	129

(a) Luminosity lightcurves not corrected for host extinction

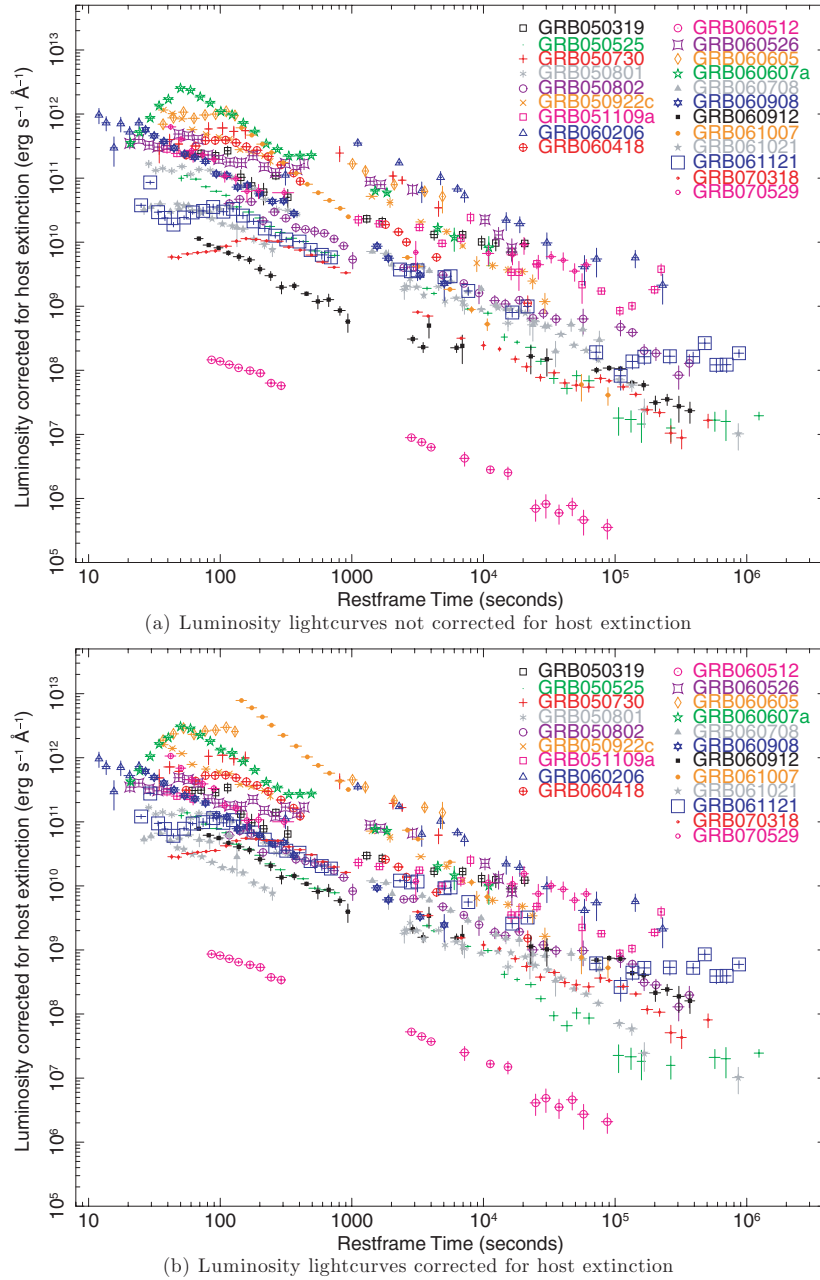(b) Luminosity lightcurves corrected for host extinction

Figure 5. The luminosity light curves for the 21 light curves in the sample with spectroscopic or photometric redshifts. Panel A shows the luminosity light curves before correction for the host extinction whereas panel B shows the luminosity light curves after correction for the host extinction. The grey light curves are the light curves with photometric redshifts.

5 DISCUSSION

In this section, we will discuss the possible mechanisms that could produce the rising behaviour of the early afterglow viewed in the observer frame before 500 s, and discuss the late afterglow from 500 s onwards. We will also discuss the implications of the luminosity distribution and compare the UVOT light curves with the XRT canonical light-curve model.

5.1 The early UVOT afterglow

There are several physical mechanisms and geometric scenarios that may produce a rise in the early optical afterglow. In this section,

the following mechanisms and scenarios will be discussed: (i) passage of the peak synchrotron frequency of the forward shock $\nu_{m,f}$, through the observing band, (ii) a reverse shock, (iii) decreasing extinction with time, (iv) the onset of the forward shock in the cases of an isotropic outflow or a jet viewed in a region of uniform energy density, (v) the rise produced by an off-axis jet, which may be structured, and finally, (vi) a two component outflow.

5.1.1 Passage of the synchrotron frequency, $\nu_{m,f}$

The first mechanism, the passage of the peak frequency of the forward shock which moves with time as $\nu_{m,f} \propto t^{-3/2}$, through the
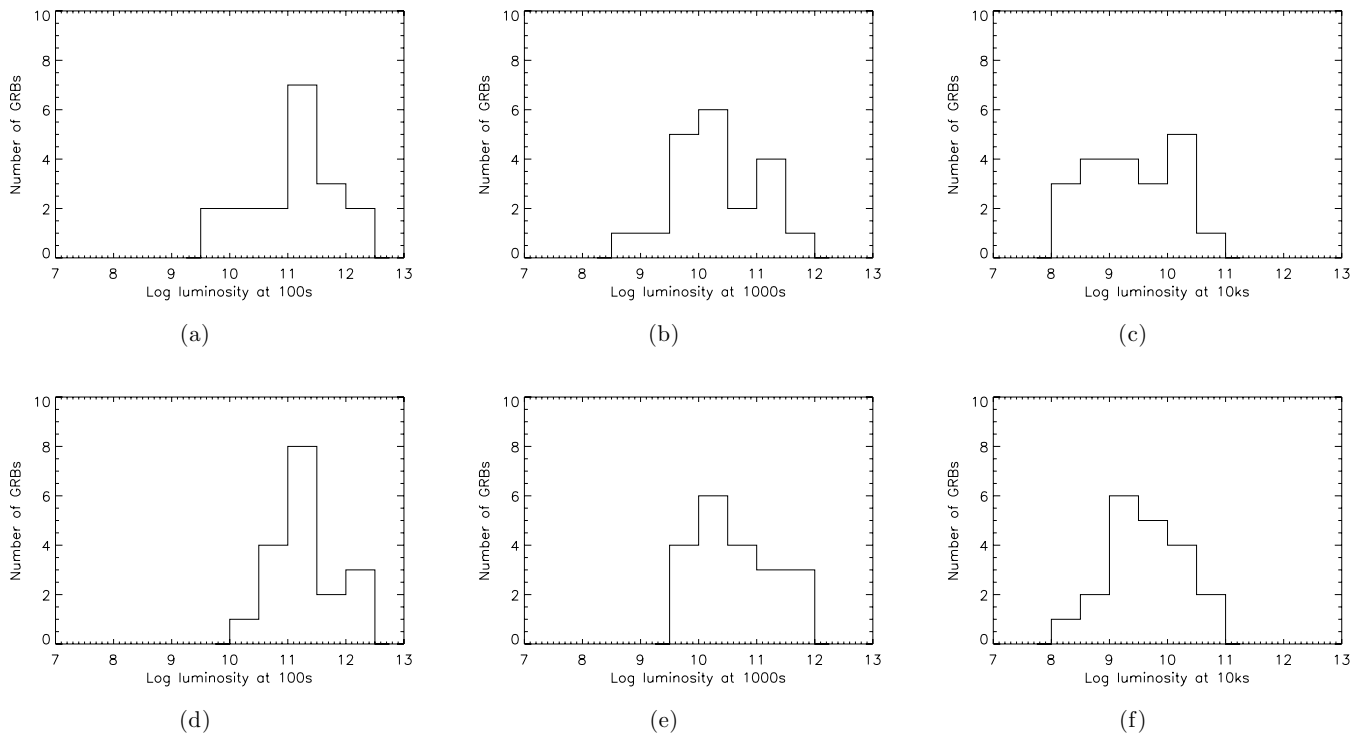
Figure 6. Luminosity distributions. The luminosities in panels (a) to (c) show the luminosities at rest frame 100 s, 1000 s and 10 ks that have not been corrected for host extinction. Panels (d) to (f) show the luminosity distributions at the same epochs, but with the light curves corrected for host extinction.
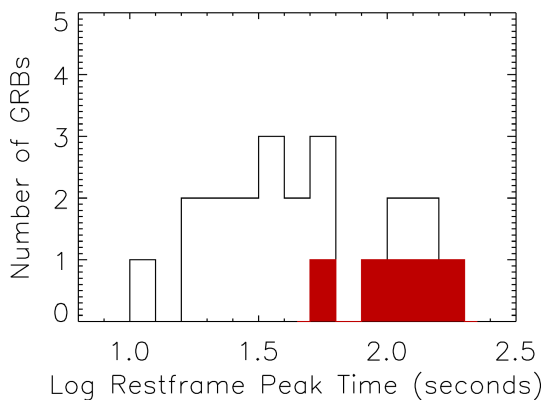

Figure 7. Distribution of the rest-frame peak times. The red filled area represents the GRBs with known rest-frame peak times, whereas the unfilled area contains the GRBs with known rest-frame peak times and those GRBs with only upper limits to their peak time. Only 21 GRBs, for which luminosity light curves were produced, are included in this figure.
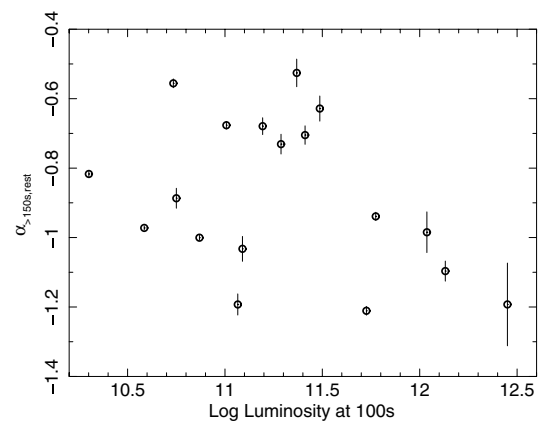

Figure 8. Temporal index determined from the light curves in the rest frame from 150 s onwards, shown against luminosity of the light curves at 100 s.

observing band, is expected to produce a chromatic peak in the optical light curve evolving from the shortest wavelengths through to the longest wavelengths. For five of the light curves with a peak, the UVOT observed the majority of the rise and the peak during the two finding chart exposures observed in white and v (see Fig. 9). If the peak were due to the passage of the synchrotron frequency, a stepped decrease in flux would be observed in the normalized light curves at the transition between the white and v observations, which has not been observed in any of these GRBs. For the sixth GRB with an observed peak, GRB 050730, the rise was observed in the v and b filters. If the passage of $\nu_{m,f}$ was the cause of this rise, the afterglow would appear to be brighter in the b filter than in the v filter during

the rise, and begin to decay earlier. However, the afterglow is not brighter in the b filter than in the v filter during the rise. Therefore, the passage of $\nu_{m,f}$ through the optical band is not responsible for any of the peaks observed in these optical afterglows.

During the passage of ν_m from the shortest wavelengths through to the longest wavelengths, the spectrum of the optical afterglow changes (assuming slow cooling) from $\nu^{1/3}$, for $\nu < \nu_m$, to $\nu^{-(p-1)/2}$, for $\nu_m < \nu < \nu_c$ (Sari, Piran & Narayan 1998). As ν_m passes from high to lower frequencies, there will be a change in colour. The colour change between the white and v filters can be calculated using the central wavelengths of the white and v filters, given in Poole et al. (2008), converted into frequency: $\nu_{white} = 8.64 \times 10^{14}$, $\nu_v = 5.49 \times 10^{14}$ Hz and assuming $p = 2.3$, where p is the electron energy index. The colour change between white and v as ν_m
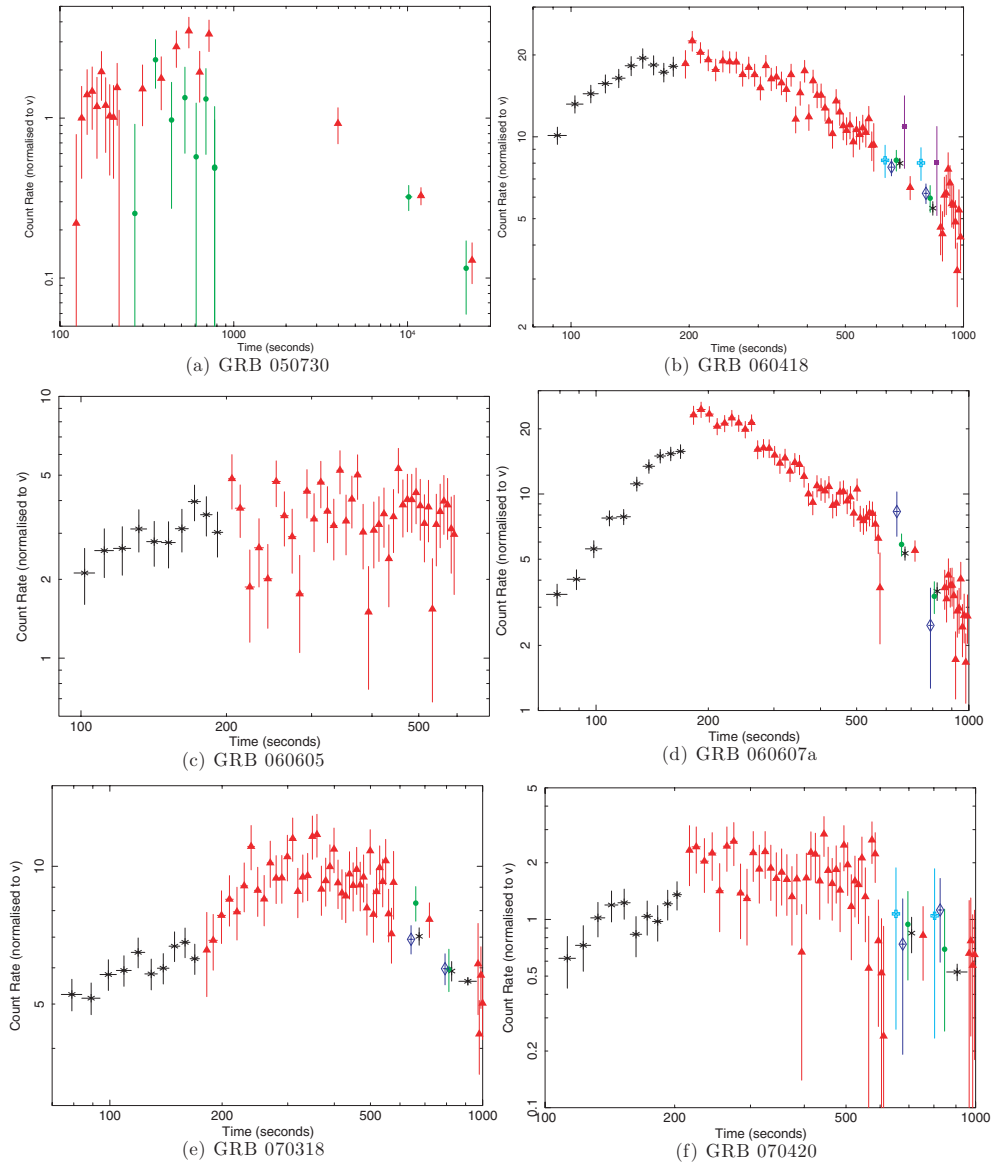
Figure 9. The early normalized light curves for the six GRBs with observed rises. GRB 050730 is the only GRB observed to rise that was not viewed with the white filter. Key: black star = white; red filled triangle = v; green circle = b; blue diamond = u; light blue cross = $uvw1$; pink hexagon = $uvm2$ and purple square = $uvw2$.

moves from above the white frequency to below the v frequency is 0.48 mag. In the light curves of Fig. 9, which have been normalized using the late-time data, the colour difference between the white and v filter after the peak is zero. None of the five light curves, in Fig. 9, with early white and v observations, shows such a large offset between the light curves in two filters during the rise. Furthermore, the equation for $\nu_{m,f}$ in a constant density medium, as given by Zhang et al. (2006), as

$$\nu_{m,f} = (6 \times 10^{15} \text{ Hz})(1 + z)^{1/2} E_{52}^{1/2} \epsilon_e^2 \epsilon_B^{1/2} (t/1d)^{-3/2}, \quad (2)$$

where $E_{52} = 10^{52}E$ is the isotropic energy in units of 10^{52} erg, ϵ_e is the fraction of energy in the electrons, ϵ_B is the fraction of energy in the magnetic field, z is the redshift and t is the time. Assuming ϵ_e and ϵ_B are not evolving with time and given the time t_1 at which $\nu_{m,f}$ is at a given frequency ν_1, the time t_2 at which $\nu_{m,f}$ is at the frequency ν_2 is given by $t_2 = t_1(\nu_2/\nu_1)^{(-2/3)}$. Using the central wavelengths of the white and v filters, the v filter should peak 1.35 times later

than the white filter. There does not appear to be any time difference between the peak in the white and v filters in the five light curves shown in Fig. 9, therefore, the passage of ν_m through the optical band is not the cause of the rise in the optical band.

For $\nu_{m,f}$, to have passed below the v filter (5402 Å) by the time the UVOT has begun observations ($t \sim 100$ s), using $\langle E_{k,\text{iso}} \rangle = 1.5 \times 10^{54}$ erg and $\langle z \rangle = 2.21$, then $\epsilon_e^2 \epsilon_B^{1/2} < 1.7 \times 10^{-5}$. The values ϵ_e and ϵ_B provided in Panaitescu & Kumar (2002) for 10 GRBs give values for $\epsilon_e^2 \epsilon_B^{1/2}$ ranging from 3×10^{-3} to 2×10^{-7}, suggesting that 1.7×10^{-5} is consistent with values found for other GRBs.

5.1.2 The reverse shock

Considering a constant density medium, there are two main cases of the reverse shock that depend on the position of the peak synchrotron

frequency of the reverse shock $\nu_{m,r}$ relative to the optical band ν_{opt}. If $\nu_{m,r} < \nu_{opt}$ then the light curve produced by the reverse shock is expected to decay immediately after the peak with $\alpha = (3p + 1)/4$ (Zhang, Kobayashi & Mészáros 2003), where p is the electron energy index. The value of p is typically taken to lie between 2 and 3, therefore α is expected to range between $\alpha = -1.75$ for $p = 2$ and $\alpha = -2.5$ for $p = 3$. Within the sample, GRB 050726, GRB 061007 and GRB 070529 are the only GRBs with decays before 500 s that are consistent at 2σ with the slowest expected reverse-shock decay index $\alpha = -1.75$; GRB 050726 has a decay of $\alpha = -2.67 \pm 0.80$, GRB 061007 decays with $\alpha = -1.63 \pm 0.11$ and GRB 070529 decays with $\alpha = -1.64 \pm 0.14$. The other light curves in the sample are shallower than the reverse-shock prediction with $>2\sigma$ confidence. The second case arises if $\nu_{m,r} > \nu_{opt}$, then immediately after the peak there is an intermediate stage where $\alpha \sim -0.5$, which is followed by $\alpha = (3p + 1)/4$. In the sample, there are seven GRBs that before 500 s have temporal indices consistent with $\alpha = -0.5$ at 2σ confidence. However, of these GRBs only GRB 060223a has a decay after 500 s ($\alpha = -1.53 \pm 0.60$) that is consistent at the 2σ level with the slowest expected reverse-shock decay index $\alpha = -1.75$.

The reverse shock in a wind medium is expected to produce a much steeper decay immediately after the peak with $\alpha \sim -3.5$ (Kobayashi, Mészáros & Zhang 2004). Only GRB 050726 has a value of $\alpha_{<500\,s}$, which is consistent to within 2σ confidence. All other GRBs are inconsistent at $>5\sigma$.

The inconsistency of the temporal indices of the GRBs in this sample to the temporal decay expected during a reverse shock for both types of medium implies that the reverse shock is not the main contributor to the optical emission at early times, and therefore is not responsible for the rise. Still the reverse shock is expected to occur for all relativistic outflows that interact with the external medium. For a number of GRBs, the reverse shock may not be observed as it can be suppressed by high levels of magnetization in the outflow (Zhang et al. 2006; Giannios, Mimica & Aloy 2008) or if the forward and reverse shocks have comparable energy, the sharp decay in the reverse shock may be masked by the flux produced by the forward shock (McMahon, Kumar & Piran 2006; Mundell et al. 2007).

5.1.3 Dust destruction

If there are high levels of extinction at the beginning of the afterglow (Klotz et al. 2008, and references within), the light curve produced would be dim and reddened at the beginning. As the dust is destroyed by the radiation, a chromatic peak would be observed as the afterglow brightens and becomes less red. The bluer filters would be expected to rise more steeply when compared to the red filters as would the white filter, because the sensitivity of this filter is skewed to the blue. However, the amount of dust destroyed is highly dependent on the environment of the GRB, in particular to the density and the size of the region surrounding the progenitor, and simulations suggest that most of the dust destruction is expected to occur within the first few tens of seconds after the trigger (Perna & Lazzati 2002). Therefore, it is unlikely that the UVOT is observing the afterglow while dust destruction is occurring.

However, as the duration of dust destruction and the quantity of dust destroyed are only theoretical predictions, we must rule out dust destruction using observations. Therefore, the six UVOT light curves with a rise were examined to see if the bluer filters, including white, rise more steeply when compared to the v filter.

The UVOT observed five of the light curves in white and v (the reddest UVOT filter) during the rise (see Fig. 9). GRB 060607a has the only light curve where there appears to be a significant excess in v compared with the white filter. However, the H-band light curve given in Molinari et al. (2007) rises at the same rate as the UVOT light curve, which was observing in white during the rise. If dust destruction was the cause of the rise, the H band would be expected to rise less steeply than the UVOT light curve. The sixth rising GRB, GRB 050730, was observed with the v and b filters during the rise and peak. If the peak in this case were due to dust destruction, an excess in v compared to b would be observed. However, the light curves of the v and b filters are consistent within 1σ errors. Therefore, there is no evidence to suggest that dust destruction is the cause of the rise for this GRB or for any of the GRBs in this sample.

5.1.4 Start of the forward shock

At the start of the forward shock, a rise will be observed in the light curves as the jet ploughs into the external medium (Sari & Piran 1999). The light curves for an observer viewing within a uniform jet, or within a cone of uniform energy density, will be the same as those observed within an isotropic outflow Granot et al. (2002. and references within). The temporal index of the rise will vary according to the thickness of the shell and the density of the external medium. Assuming the synchrotron self-absorption frequency $\nu_a < \nu_{opt}$, then the thickness of the shell and the density profile of the external medium affect the rate at which the light curve rises. For the thick shell case, the temporal index is $\alpha = 1$ for a constant density medium, or $\alpha = 1/9$ for a wind medium. For the thin shell case, in a constant density medium, the temporal index is either $\alpha = 2$ for $\nu_c < \nu_{opt}$ or $\alpha = 3$ for $\nu_c > \nu_{opt}$. Lastly, the temporal index is $\alpha = 0.5$ if the shell is thin and in a wind medium (Panaitescu & Vestrand 2008).

Given the peak time, the Lorentz factor Γ of the shell at the moment of the peak for a constant density medium, can be derived using the following equation (Sari 1997; Molinari et al. 2007):

$$\Gamma(t_{peak}) = \left[\frac{3E(1 + z)^3}{32\pi n m_p c^5 \eta (t_{peak}/100\,s)^3} \right]^{1/8}, \qquad (3)$$

where t_{peak} is the peak time, η is the radiative efficiency and n is the density of the medium. Here, we will assume $\eta = 0.2$ and $n = 1\,cm^{-3}$. However, changing the values of η and n has a minor effect on the final values of $\Gamma(t_{peak})$ as the dependence of $\Gamma(t_{peak})$ on these parameters is small: $\Gamma(t_{peak}) \propto (\eta n)^{-1/8}$. For each GRB, the k-corrected energy, given in Table 3, was used in the above equation to determine $\Gamma(t_{peak})$ and the resulting values of $\Gamma(t_{peak})$ for the individual GRBs can be found in Table 3. The mean of the $\Gamma(t_{peak})$ for the GRBs with a peak in their light curve is $\langle \Gamma(t_{peak}) \rangle \sim 180$, which is consistent with the expectation that the initial Lorentz factor of the jet Γ_0, where $\Gamma_0 \sim 2\Gamma(t_{peak})$ (Panaitescu & Kumar 2000; Meszaros 2006), of GRBs is >100 (Fenimore, Epstein & Ho 1993). For the GRBs where only an upper limit to their peak time is known, the mean value for $\Gamma(t_{peak})$ is a lower limit, $\langle \Gamma(t_{peak}) \rangle > 230$. This suggests that the GRBs with observed peaks typically have lower Lorentz factors than the GRBs with upper limits to their peak times.

Using the derived values of $\Gamma(t_{peak})$, it is possible to deduce two more quantities: the isotropic-equivalent mass of the baryonic load $M_{fb} = E/(\Gamma_0 c^2)$ and the deceleration radius $R_{dec} \simeq 2ct_{peak} \Gamma(t_{peak})^2/(1 + z)$ (Molinari et al. 2007). These quantities were determined for each GRB and the results are given in Table 6. The

Table 6. Properties of the GRBs derived assuming the rise of the forward shock is the cause of the rise observed in the UVOT light curves. The initial Lorentz factors were determined using the peak times and equation (1) of Molinari et al. (2007). Where only an upper limit to the peak time is known, only a lower limit to the Lorentz factor is given. The fraction of mass as baryons and the deceleration radius are determined using the Lorentz factor.

GRB	Lorentz factor at peak	M_{fb}	R_{dec}
050319	>168	< 2.40 e − 04	<9.33 e + 16
050525	>179	<2.49 e − 04	<9.25 e + 16
050730	174	6.18 e − 03	2.72e+17
050801	>275	<7.81 e − 04	<1.17 e + 17
050802	>156	<1.05 e − 03	<1.56 e + 17
050922c	>308	<3.91 e − 03	<1.93 e + 17
051109a	>236	<7.61 e − 04	<1.22 e + 17
060206	>338	<2.83 e − 04	<7.80 e + 16
060223a	>409	<3.06 e − 03	<1.62 e + 17
060418	193	4.27 e − 03	2.32e+17
060512	>72	<1.95 e − 06	<2.48 e + 16
060526	>247	<1.55 e − 04	<7.09 e + 16
060605	177	1.82 e − 03	1.80e+17
060607a	220	2.30 e − 03	1.81e+17
060708	>256	<4.14 e − 04	<9.72 e + 16
060908	>231	<2.27 e − 04	<8.23 e + 16
060912	>235	<3.00 e − 03	<1.94 e + 17
061007	>126	<4.42 e − 04	<1.26 e + 17
061021	>173	<1.56 e − 04	<7.99 e + 16
061121	>337	<2.28 e − 03	<1.57 e + 17
070318	103	2.38 e − 04	1.09e+17
070420	228	7.84 e − 03	2.69e+17
070529	>234	<7.71 e − 04	<1.23 e + 17

mean mass of the baryonic load and the mean deceleration radius for the GRBs with an observed rise are $\langle M_{fb} \rangle = 3.8 \times 10^{-3}$ M$_\odot$ and $\langle R_{dec} \rangle = 2.1 \times 10^{17}$ cm and for the GRBs without an observed rise the quantities are $\langle M_{fb} \rangle < 1.1 \times 10^{-3}$ M$_\odot$ and $\langle R_{dec} \rangle < 1.2 \times 10^{17}$ cm. The deceleration radii are in agreement with $R_{dec} \sim 10^{16}$cm as predicted by theory (Rees & Meszaros 1992). Therefore, the forward shock is consistent with our observations.

5.1.5 Off-axis and structured outflows

A rise may be produced in the light curve if the observer's viewing angle is $\theta_{obs} > \theta$, where θ_{obs} is the observers viewing angle and θ is the half-opening angle of the jet. In the case of a uniform jet, the ejecta are released into a cone of angle θ and due to relativistic effects, the emission in the jet is beamed as Γ^{-1}. If $\theta_{obs} > \theta$, then the emission is strongly beamed away from the observer, but as Γ decreases, the emission entering the line of sight increases and the observed light curve will rise. The light curve will peak when $\Gamma \sim (\theta_{obs} - \theta)^{-1}$ (Granot et al. 2002). Larger observing angles will view a later peak and the peak magnitude will be lower (Granot, Ramirez-Ruiz & Perna 2005). A structured jet, in which the energy per solid angle decreases around a uniform core of angular size θ_c, viewed off-axis ($\theta_{obs} > \theta_c$) can produce a rise in the optical afterglow, where the behaviour of the rise may vary depending on the distribution of energy around the core. In this case, the more diffuse the energy per solid angle, the slower the rise and the later the peak time (Granot et al. 2002; Panaitescu & Vestrand 2008). The peak time of the light curve is also dependent on the viewing angle of the jet and the peak will occur when $\Gamma \sim (\theta_{obs} - \theta_c)^{-1}$.

5.1.6 Two component outflows

A two component outflow consists of a narrow jet surrounded by a wide jet. The narrow component will be denoted by a subscript n and the wide component will be denoted by a subscript w. Both components move at relativistic speeds, but the narrow jet will have a larger Γ (i.e. $\Gamma_w < \Gamma_n$) and the wide component will have a larger half-opening angle than the inner narrow jet (i.e. $\theta_w < \theta_n$). The optical emission is expected to be produced either within the wide component (Oates et al. 2007; de Pasquale et al. 2008) or more traditionally from both the narrow and wide components (Huang et al. 2004; Peng, Königl & Granot 2005).

In the case where the optical emission is only produced by the wide component, the rise observed will occur as in Section 5.1.4, provided that the jet is viewed within $1.5\theta_w$, as has been demonstrated by Granot et al. (2002). At angles larger than $1.5\theta_w$, the peak of the optical light curve will occur when $\Gamma \sim (\theta_{obs} - \theta_w)^{-1}$. This model of the two component outflow could produce the rises observed in this sample.

In the case where the optical emission is produced in both the narrow and the wide components, the dominance of emission from one component over the other depends mostly on the energy within each component and on the viewing angle of the observer (for a more detailed description, see Peng et al. 2005). However, in this case as the emission is produced in both components, it is likely that on-axis and off-axis viewers will observe two peaks. This effect is not seen in the UVOT light curves in this paper and therefore, the jet is unlikely to have two components where both produce optical/UV emission.

5.2 The late UVOT afterglow

A correlation has been observed between the observed magnitude at 400 s and the decay after 500 s. However, there is no significant evidence from a Spearman rank test performed between $\alpha_{>150s, rest}$ and the luminosity in the rest frame at 100 s, for a similar correlation in the rest frame. For an off-axis jet, a correlation is expected between the luminosity and the decay of the light curve when the viewing angle is changed, with fainter, shallower afterglows having a larger viewing angle (Panaitescu & Vestrand 2008). As these data do not show a strong correlation of this type, this suggests that the outflows are viewed within the half-opening angle θ or within a core of uniform energy density θ_c. This supports the idea that the start of the forward shock produces the rises observed in the UVOT light curves. However, this does not give an indication of the geometry of the jet which may be uniform, comprises two components, or structured.

5.3 UVOT afterglow luminosity

The luminosity distribution found in this work shows no evidence for bimodality, which is in contradiction with the results of Nardini et al. (2006), Nardini, Ghisellini & Ghirlanda (2008), Liang & Zhang (2006) and Kann et al. (2007), who all claim a bimodal distribution within their samples. However, the lack of evidence for bimodality within the distributions in this sample is consistent with the work of Cenko et al. (2008) and Melandri et al. (2008). Cenko et al. (2008) present a luminosity distribution at 1000 s in the rest frame from a sample of 17 GRBs, with known redshift, observed with the Palomar 60 in telescope. Their distribution shows no evidence for bimodality. Melandri et al. (2008) produce three luminosity distributions for 16 optical afterglows observed with

the Liverpool and Faulkes telescopes. They find a single-peaked luminosity distribution for three rest-frame epochs: 10 min, 0.5 d and 1 d, which are well fit by a lognormal function. Melandri et al. (2008) do not correct their light curves for host extinction, but as discussed in this paper the correction for host extinction appears to have minimal effect on the luminosity distribution. Therefore, it is possible to compare the distributions of Melandri et al. (2008) with the distributions produced with this sample.

5.4 Comparison of the XRT and UVOT canonical light curves

There are three segments which are usually found in X-ray light curves within the first $\sim 10^5$ s (Zhang et al. 2006; Nousek et al. 2006). The first segment is a fast, early decay with $-5 < \alpha_{X1} < -3$, typically ending within 100–1000 s after the trigger. The fast decay is thought to be caused by the tail of the prompt emission (Zhang et al. 2006; Nousek et al. 2006). The second segment is shallow with $-1.0 < \alpha_{X2} < -0.5$ (although this range should now be considered as $-1.0 < \alpha_{X2} < 0.0$, Liang, Zhang & Zhang 2007), ceasing between 1000 and 10 000 s and attributed to energy injection (Zhang et al. 2006; Nousek et al. 2006). The third segment decays as $-1.5 < \alpha_{X3} < -1$ and is expected to occur at the end of energy injection (Zhang et al. 2006; Nousek et al. 2006).

The range in temporal index of the optical light curve before 500 s, taken as the mean plus or minus the dispersion, is $-1.17 < \alpha < 0.21$. This range is clearly inconsistent with the first segment of the XRT canonical light curve. The range of temporal index before 500 s is most similar to the range of the second segment of the XRT canonical model. However, none of the XRT canonical light curve segments indicates rising behaviour for the X-ray light curves. Applying the theoretical interpretations for the individual segments of the XRT canonical light curve, provided by Zhang et al. (2006) and Nousek et al. (2006), to the UVOT canonical light curve suggests that before 500 s, the emission producing the optical light curves is from the forward shock and a number of the UVOT afterglows during this period are energy injected. The lack of corresponding rising behaviour in the X-ray light curves, presuming an achromatic rise ($\nu_m < \nu_{opt}$), suggests that the rise of the forward shock is masked in the X-rays, possibly by the contribution of the prompt emission. This is consistent with the model of Willingale et al. (2007) who suggest that the steep and shallow decays of the X-ray light curves are dominated by the prompt emission and afterglow emission respectfully, and they do not observe the rise of the afterglow emission as this is masked by the prompt emission.

In Section 4, the light curves after 500 s were fitted with power laws and broken power laws. The GRBs which were best fitted by broken power laws are discussed separately. For the optical light curves that decay as power laws, the range in decay is $-1.22 < \alpha < -0.52$. Like the range in decay before 500 s, the range in decay after 500 s is most similar to the decay range of the second segment of the XRT canonical model. Assuming the same reasoning as for the XRT segments, this suggests that after 500 s the optical light curves are consistent with emission from the forward shock and most of these are energy injected.

For the four GRBs that are best fit with a broken power law after 500 s, the range in temporal decay before the break is $-0.74 < \alpha < -0.46$, which is consistent with the range given for the second segment of the canonical XRT model. This suggests that before the break the optical light curves are energy injected. The range in temporal decay after the break is $-1.72 < \alpha < -1.34$, which is consistent with the third decay of the XRT canonical light curve,

which has been suggested to be the decay following the end of energy ejection.

6 CONCLUSIONS

In this paper, we systematically reduced and analysed a sample of 27 GRBs, which met a strict set of selection criteria. We note that the temporal behaviour of the optical afterglows in the sample is varied, with the greatest variation occurring in the early phase of the light curves: before 500 s, the light curves may rise or decay. The mean for $\alpha_{<500\,s}$ is $-0.48^{+0.15}_{-0.19}$ with a dispersion of $0.69^{+0.19}_{-0.06}$. However, after 500 s, all the light curves decay. The light curwere fitted with power laws and broken power laws. A broken power law was deemed to be an improvement, if the χ^2/d.o.f. decreased and the probability of chance improvement was small (<1 per cent) and in five cases a broken power law was considered a better fit. The mean decay index after 500 s, when including only those that decay with a single power law, is $-0.87^{0.10}_{-0.09}$ with a dispersion of $0.35^{+010}_{-0.04}$. There is a correlation at 99.8 per cent probability, between the magnitude at 400 s and the temporal decay after 500 s, with the brightest optical afterglows decaying the fastest.

We investigated the cause of the rising behaviour in the early afterglow and discussed the following physical mechanisms and geometric scenarios: the passage of the synchrotron frequency ν_m, reverse shock, dust destruction, the start of the forward shock, the viewing angle of a (possibly structured) jet and a two component outflow. The rise in the optical light curves may be attributed to either the start of the forward shock, or to an off-axis viewing angle where the observer sees an increasing amount of emission as the Lorentz factor of the jet decreases. We also investigated the correlation between magnitude and decay after 500 s. We determined that a correlation observed between the magnitude at 400 s and the decay after 500 s is only weakly dependent on redshift. A Spearman rank test performed between the luminosities at 100 s and the decay after 150 s in the rest frame did not reveal a significant correlation. However, a luminosity–decay correlation would be expected for jets viewed off-axis, where the more off-axis the jet, the fainter and shallower the light curve. We do not observe a strong correlation of this type, suggesting that the optical light curves are produced by jets viewed on-axis and the rise observed in the optical light curves is caused by the start of the forward shock.

We produced luminosity light curves for the 21 GRBs in the sample with known redshift. The luminosity light curves were produced at a common wavelength of 1600 Å in the rest frame. We find that the logarithmic distribution of the luminosities at three rest-frame epochs: 100 s, 1000 s and 10 ks do not show evidence for bimodality. Correcting the light curves for the host extinction increases the mean luminosities of the distributions, but does not considerably alter their appearance and the change in standard deviations of the logarithmic luminosity distributions is no greater than 0.08 for any of the three epochs. The lack of evidence for bimodality is consistent with the findings of Melandri et al. (2008) and Cenko et al. (2008).

Finally, we compared the temporal behaviour of the optical afterglows in this sample with the XRT canonical model. We have found that the temporal indices before 500 s and the temporal indices of the light curves after 500 s are most consistent with the shallow decaying segment of the XRT canonical model. Nousek et al. (2006) and Zhang et al. (2006) suggest that the shallow decay segment of the XRT canonical model is energy injected. This would suggest that the optical light curves are energy injected as well. The lack

of rises observed in X-ray afterglows could be due to the prompt emission masking them.

REFERENCES

Band D., Matteson J., Ford L., Schaefer B., Palmer D., Teegarden B., Cline T., Briggs M., 1993, ApJ, 413, 281
Barthelmy S. D. et al., 2005, Space Sci. Rev., 120, 143
Berger E., Kulkarni S. R., Rau A., Fox D. B., 2006, GCN, 4815
Berger E., Fox D. B., Cucchiara A., 2007, GCN, 6470
Bloom J. S., Frail D. A., Sari R., 2001, AJ, 121, 2879
Bloom J. S., Foley R. J., Kocevski D., Perley D., 2006, GCN, 5217
Bloom J. S., Perley D. A., Chen H. W., 2006, GCN, 5826
Burrows D. N. et al., 2005, Space Sci. Rev., 120, 165
Burrows D. N. et al., 2007, in Siegmund O. H. W., ed., Proc. SPIE Vol. 6686, UV, X-ray and Gamma-Ray Space Instrumentation for Astronomy XV. SPIE, Bellingham, p. 668607
Chen H.-W., Thompson I., Prochaska J. X., Bloom J., 2005, GCN, 3709
Cenko S. B. et al., 2008, preprint (arXiv:0808.3983)
D'Alessio V., Piro L., Rossi E. M., 2006, A&A, 460, 653
de Pasquale M. et al., 2008, MNRAS, 392, 153
Fenimore E. E., Epstein R. I., Ho C., 1993, A&AS, 97, 59
Foley R. J., Chen H.-W., Bloom J., Prochaska J. X., 2005, GCN, 3483
Fynbo J. P. U. et al., 2005, GCN, 3749
Fynbo J. P. U., Limousin M., Castro Cerón J. M., Jensen B. L., Naranen J., 2006, GCN, 4692
Giannios D., Mimica P., Aloy M. A., 2008, A&A, 478, 747
Golenetskii S., Aptekar R., Mazets E., Pal'Shin V., Frederiks D., Cline T., 2005a, GCN, 3474
Golenetskii S., Aptekar R., Mazets E., Pal'Shin V., Frederiks D., Cline T., 2005b, GCN, 4030
Golenetskii S., Aptekar R., Mazets E., Pal'Shin V., Frederiks D., Cline T., 2005c, GCN, 4238
Golenetskii S., Aptekar R., Mazets E., Pal'Shin V., Frederiks D., Cline T., 2006a, GCN, 5837
Golenetskii S., Aptekar R., Mazets E., Pal'Shin V., Frederiks D., Cline T., 2006b, GCN, 5570
Golenetskii S., Aptekar R., Mazets E., Pal'Shin V., Frederiks D., Cline T., 2006c, GCN, 5722
Golenetskii S., Aptekar R., Mazets E., Pal'Shin V., Frederiks D., Cline T., 2006d, GCN, 5748
Golenetskii S., Aptekar R., Mazets E., Pal'Shin V., Frederiks D., Ulanov M., Cline T., 2006e, GCN, 4989
Golenetskii S., Aptekar R., Mazets E., Pal'Shin V., Frederiks D., Cline T., 2007, GCN, 6344
Granot J., Panaitescu A., Kumar P., Woosley S. E., 2002, ApJ, 570, L61
Granot J., Ramirez-Ruiz E., Perna R., 2005, ApJ, 630, 1003
Huang Y. F., Wu X. F., Dai Z. G., Ma H. T., Lu T., 2004, ApJ, 605, 300

Jakobsson P. et al., 2006a, A&A, 460, L13
Jakobsson P., Fynbo J. P. U., Tanvir N., Rol E., 2006b, GCN, 5716
Jakobsson P., Levan A., Chapman R., Rol E., Tanvir N., Vreeswijk P., Watson D., 2006c, GCN, 5617
Jaunsen A. O., Fynbo J. P. U., Andersen M. I., Vreeswijk P., 2007, GCN, 6216
Kalberla P. M. W., Burton W. B., Hartmann D., Arnal E. M., Bajaja E., Morras R., Pöppel W. G. L., 2005, A&A, 440, 775
Kann D. A. et al., 2007, preprint (arXiv:0712.2186)
Klotz A. et al., 2008, A&A, 483, 847
Kobayashi S., Mészáros P., Zhang B., 2004, ApJ, 601, L13
Ledoux C., Vreeswijk P., Smette A., Jaunsen A., Kaufer A., 2006, GCN, 5237
Liang E., Zhang B., 2006, ApJ, 638, L67
Liang E.-W., Zhang B.-B., Zhang B., 2007, ApJ, 670, 565
Maccacaro T., Gioia I. M., Wolter A., Zamorani G., Stocke J. T., 1988, ApJ, 326, 680
McMahon E., Kumar P., Piran T., 2006, MNRAS, 366, 575
Melandri A. et al., 2008, ApJ, 686, 1209
Meszaros P., 2006, Rep. Prog. Phys., 69, 2259
Meszaros P., Rees M. J., 1997, ApJ, 476, 232
Molinari E. et al., 2007, A&A, 469, L13
Mundell C. G. et al., 2007, ApJ, 660, 489
Nardini M., Ghisellini G., Ghirlanda G., Tavecchio F., Firmani C., Lazzati D., 2006, A&A, 451, 821
Nardini M., Ghisellini G., Ghirlanda G., 2008, MNRAS, 386, L87
Nousek J. A. et al., 2006, ApJ, 642, 389
Oates S. R. et al., 2007, MNRAS, 380, 270
Panaitescu A., Kumar P., 2000, ApJ, 543, 66
Panaitescu A., Kumar P., 2002, ApJ, 571, 779
Panaitescu A., Vestrand W. T., 2008, MNRAS, 387, 497
Pei Y. C., 1992, ApJ, 395, 130
Peng F., Königl A., Granot J., 2005, ApJ, 626, 966
Perna R., Lazzati D., 2002, ApJ, 580, 261
Peterson B., Schmidt B., 2006, GCN, 5223
Poole T. S. et al., 2008, MNRAS, 383, 627
Prochaska J. X., Chen H.-W., Bloom J. S., Falco E., Dupree A. K., 2006, GCN, 5002
Quimby R., Fox D., Hoeflich P., Roman B., Wheeler J. C., 2005, GCN, 4221
Rees M. J., Meszaros P., 1992, MNRAS, 258, 41
Rees M. J., Meszaros P., 1994, ApJ, 430, L93
Rol E., Jakobsson P., Tanvir N., Levan A., 2006, GCN, 5555
Roming P. W. A. et al., 2005, Space Sci. Rev., 120, 95
Roming P. W. A. et al., 2009, 690, 163
Sakamoto T. et al., 2008a, ApJS, 175, 179
Sakamoto T. et al., 2008b, ApJ, 679, 570
Sari R., 1997, ApJ, 489, L37
Sari R., Piran T., 1999, ApJ, 520, 641
Sari R., Piran T., Narayan R., 1998, ApJ, 497, L17
Sari R., Piran T., Halpern J. P., 1999, ApJ, 519, L17
Schady P. et al., 2009, MNRAS, submitted
Schlegel D. J., Finkbeiner D. P., Davis M., 1998, ApJ, 500, 525
Zhang B., Kobayashi S., Mészáros P., 2003, ApJ, 595, 950
Zhang B., Fan Y. Z., Dyks J., Kobayashi S., Mészáros P., Burrows D. N., Nousek J. A., Gehrels N., 2006, ApJ, 642, 354

This paper has been typeset from a TEX/LATEX file prepared by the author.